International Journal of Heat and Mass Transfer 188 (2022) 122639

Contents lists available at ScienceDirect

International Journal of Heat and Mass Transfer

journal homepage: www.elsevier.com/locate/hmt

Deep convolutional autoencoder augmented CFD thermal analysis of bearings with inter pad groove mixing

Jongin Yang, Alan Palazzolo*

Department of Mechanical Engineering, Texas A&M University, College Station, TX 77840, United States

ARTICLE INFO

Article history:
Received 18 June 2021
Revised 17 December 2021
Accepted 26 January 2022
Available online 5 February 2022

Keywords:
Thermal analysis
Rotor-bearing heat transfer
Deep learning
Groove mixing

ABSTRACT

The treatment of thermal mixing in inter pad grooves of a fluid film bearing is essential due to its influence on the heat transfer with the rotating shaft and stationary bearing. Lower fidelity models that either neglect or over approximate thermal groove mixing may lead to premature bearing or machinery failure, most commonly from babbitt thermally induced fatigue. Conventional models rely on bulk flow and thermal analyses yielding a single temperature at the groove outlet into the pad inlet. The high uncertainty of this approach carries over into downstream predictions for bearing life, stiffness and damping, and machinery vibration predictions. Contrary to a uniform temperature, CFD-Conjugate heat transfer studies reveal large gradient temperature distributions varying in both the radial and axial directions at the groove outlet, especially with jet lubrication implemented with multiple nozzles. These distributions vary continuously with time as the spinning shaft and bearing pads vibrate. A direct CFD simulation thus becomes computationally prohibitive.

The present work introduces a novel approach which yields highly detailed lubricant temperature distributions at the pad inlets in a computationally economical manner. This is implemented with a surrogate groove model via a deep convolutional autoencoder neural network based on CFD (Computational Fluid Dynamics) data. The trained Convolutional Neural Network (CNN) shows excellent prediction capability for 2D temperature distribution at a circumferential groove outlet. The trained CNN is combined with a rotor-bearing model, and the combined model is verified by full CFD results and experimental data. In addition, this approach is expanded to include various oil injection types, illustrating their detailed heat transfer to the rotating shaft and bearing.

1. Introduction

High performance turbines, compressors, pumps, turboexpanders, etc. rely on fluid film bearings for shaft load support and vibration control. The lubricant temperature in the bearing is highly affected by the method of lubrication and operating conditions. The lubricant temperature also affects viscosity which in turn affects load capacity, minimum film thickness, and stiffness and damping. Furthermore, temperature affects the mechanical integrity of the bearing, i.e. accelerated corrosion, increased thermal and vibration induced fatigue, and creep induced rippling with increased temperature. Thus, accurate bearing thermal analyses need to be conducted to properly design the machine to avoid excessive vibration and bearing thermal induced damage. Bearing and journal temperatures are highly influenced by the mixing of the cooler supply oil with the hotter carryover oil between pads. Thus, it is highly important to adapt an accurate model of the thermal flow mixing that occurs in the grooves between pads, including effects of the moving surfaces and oil injection jets. Fig. 1(a) and (b) provides an illustration of the thermal flow mixing in a generic groove region. This determines the groove outlet flow temperature distribution which is the distribution at the following pad's leading edge inlet. Therefore, the journal and pad temperatures are influenced by the thermal flow mixing between pads. The importance of this influence is widely recognized [1–4] but has been treated with highly approximate modeling due to computational time constraints. Examples of recent publications implementing simplified thermal groove models include [5–9].

Recent studies [10–12] presented a full CFD model for a bearing system, including the groove regions. However, this approach leads to excessive computation time for conducting parametric studies typically required in an industry design setting, considering geometry, nozzle configuration and operation condition variations for tilting pad bearings.

Nonlinearities, turbulence model selection, and other factors associated with solving the Navier-Stokes equations, and the poor

* Corresponding author.
E-mail address: a-palazzolo@tamu.edu (A. Palazzolo).

https://doi.org/10.1016/j.ijheatmasstransfer.2022.122639
0017-9310/

Nomenclature

T	Temperature, degC
Q	Flow rate, m^3/s
η	Non-dimensional temperature
η_k	Mixing coefficient
p	Static pressure, Pa
p'	Modified pressure, Pa
ρ	Density, kg/m^3
u_i	Fluid velocity, m/s
μ_l	Fluid dynamic viscosity, Pa·s
μ_t	Eddy viscosity, Pa·s
μ_{eff}	Effective viscosity, Pa·s
k	Turbulent kinetic energy, m^2/s^2
ω	Turbulent frequency, 1/s
γ	Turbulent intermittency
h_{tot}	Total enthalpy, J/kg
λ	Thermal conductivity, W/(m·K)
h_l	Film thickness, m
U_s	Shaft surface velocity, m/s
x_p	Pad x-coordinate at interface between fluid-film and pad, m
y_p	Pad y-coordinate at interface between fluid-film and pad, m
x_s	Shaft x-displacement, m
y_s	Shaft y-displacement, m
R_s	Shaft radius, m
h_{te}	Film thickness change by thermal deformation, m
c_p	Specific heat, J/(kg·K)
$\vec{U}$	Fluid velocity vector, m/s
K_{yy}	Non-dimensional direct stiffness coefficient
C_{yy}	Non-dimensional direct damping coefficient
k_{yy}	Direct stiffness coefficient, N/m
c_{yy}	Direct damping coefficient, N·s/m

Subscripts

in	Groove circumferential inlet
out	Groove circumferential outlet
sup	Supply oil inlet
l	Liquid (or fluid)
s	Shaft (or solid)

Acronyms

CFD	Computational Fluid Dynamics
CNN	Convolutional Neural Network
DOE	Design of Experiment
FEM	Finite Element Method
FVM	Finite Volume Method
GPU	Graphics Processing Unit
RANS	Reynolds Averaged Navier Stokes
ReLU	Rectified Linear Unit
RMSE	Root Mean Squared Error
SST	Shear Stress Transport
LEG	Leading Edge Groove
LHS	Latin Hypercube Sampling

orthogonal mesh quality which converging-wedge shaped thin-film modeling can produce, further exacerbates the computation time challenge. Thus, the conventional approaches, which apply the Reynolds model for thin-film regions, have been broadly used in industry and academic areas. This approach employs a mixing coefficient (η_k) to predict a highly simplified, approximate uniform non-dimensional temperature distribution at the groove outlet, which is the pad leading-edge.

Define the non-dimensional temperature, $\eta(\mathrm{r,z})$, by

$$\eta(r,z) = \frac{T_{out}(r,z) - T_{sup}}{T_{in} - T_{sup}} = f(Q_{in}, Q_{out}, \eta_k \ldots) \quad (1)$$

where T_{sup}, T_{in}, and T_{out} are the supply oil temperature, circumferential groove inlet temperature, and circumferential outlet temperature, respectively. The mixing coefficient is an assumed constant, typically ranging from 0.4 to 1.0, according to oil injection types. Ettles [1] proposed the simplest form of a groove model, where the non-dimensional temperature is equal to the mixing coefficient ($\eta(\mathrm{r,z}) = \eta_k$). However, the Ettles' model does not satisfy mass and energy conservation, which then compromises the temperature solution. Mitsui et al. [2] derived a mathematical expression for the temperature calculation at the pad leading edge from mass and energy balances ($\eta(\mathrm{r,z}) = \eta_k|\frac{Q_{in}}{Q_{out}}|where$, Q_{in}: circumferential groove inflow [m^3/s], and Q_{out}: circumferential groove outflow [m^3/s]). Suh and Palazzolo [3] pointed out that Mitsui's model has a limitation when Q_{in}/Q_{out} is higher than 1, and they suggested a revised form ($\eta(\mathrm{r,z}) = \min[|Q_{in}/Q_{out}|, \eta_k]$) for the non-dimensional temperature distribution at the pad leading-edge. In a recent study, Abdollahi and San Andres [4] presented a groove model from mass and energy balances, including the circumferential groove inflow, circumferential groove outflow, side leakage flow, supply oil flow, and recirculating oil flow with the groove efficiency parameter assumed from 0.1 to 0.9, instead of using the mixing coefficient. The main drawbacks of the aforementioned conventional approaches are the assumed value of the mixing coefficient, and neglect of the temperature distribution in the radial and axial directions at the circumferential groove outlet.

Proposed here is a novel machine learning approach to provide accurate pad leading edge, inlet conditions. This utilizes regression with respect to various input parameters to remove the thermal mixing coefficient's uncertainty. Machine learning techniques are becoming more popular for regression in the heat transfer area, showing reliable prediction performance. Liang et al. [13] proposed a deep neural network to calculate boiling heat transfer in helical coils, and the neural network was trained on the measured test data. Zhu et al. [14] took advantage of machine learning to predict the heat transfer of two-phase flow boiling and condensation in mini channels. In addition, machine learning techniques have been employed for the prediction of effective thermal conductivity in sands [15], dynamic thermal behavior of super-capacitor modules [16], thermal properties of composite phase change materials [17], and so on.

Yang and Palazzolo [18] applied machine learning to lessen the uncertainty of the pad film inlet temperature boundary condition, due to assuming a uniform inlet temperature mixing coefficient. The researchers used a shallow neural network for the regression of mixing coefficient based on CFD-generated data. Even though the research showed reliable generalization of the neural network, the model did not provide a 2D temperature distribution at the pad leading edge, but instead provided a single mixing coefficient for the average inlet temperature. This is inadequate for some high performance bearings that have highly varying temperatures over the pad inlets due to localized bearing cooling approaches. The temperature distribution at the pad leading edge affects the heat transfer to the rotating shaft and tilting pads, which in turn changes film thickness due to thermal growths, load capacity, minimum film thickness and stiffness and damping coefficients. The literature does not report any prior attempts to include a general 2D thermal boundary condition at the pad inlets, while utilizing a Reynolds based pressure model for the lubricant film. In this study, a deep convolutional autoencoder neural network, which consists of an encoder and decoder with convolutional layers, has been presented to predict the 2D temperature distribution at the pad leading edge, and the neural network is trained based

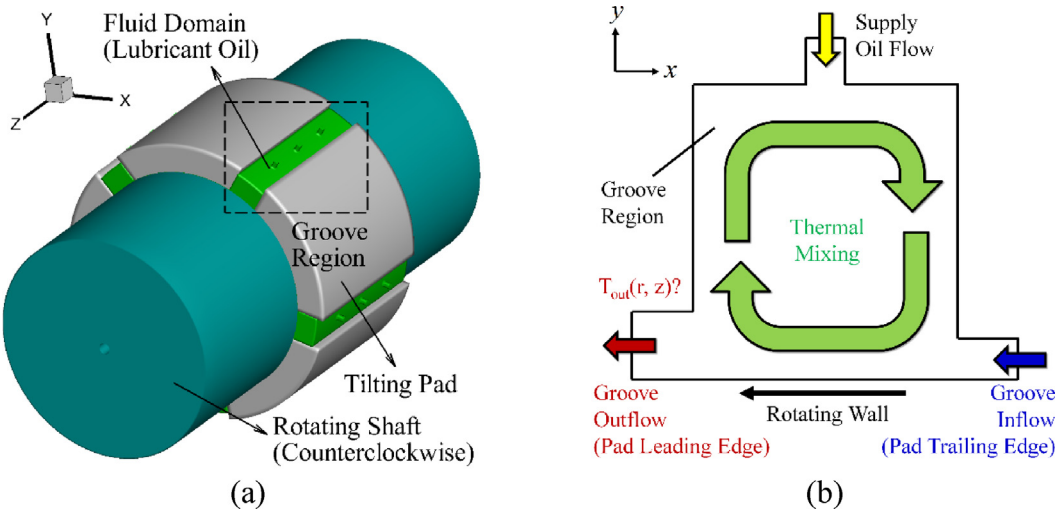

Fig. 1. Illustration of groove thermal mixing and application in rotor-bearing system; (a) rotor-tilt pad journal bearing, (b) groove thermal mixing (side view).

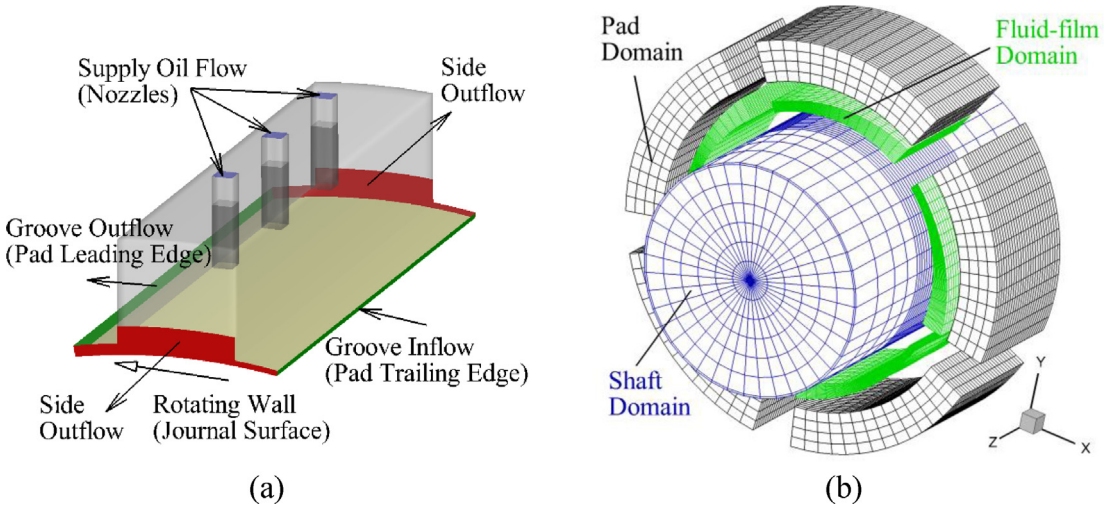

Fig. 2. Computational domains; (a) CFD groove model, (b) rotor-bearing model (45,920 elements) with Reynolds-based Fluid-film (adjusted scale for better visualization).

on CFD-generated results for the groove region. The proposed neural network shows excellent generalization performance with the adaptable design process. The trained neural network is used as a surrogate groove model, and it is combined with a thermal-elastic-hydrodynamic rotor-bearing model. The proposed model has been verified through the comparison to test data [19] and full CFD results [12] from previous studies. The accuracy limitation of the conventional, assumed constant mixing coefficient groove model is shown via comparison with high fidelity CFD results. In addition, several neural networks are trained for various types of oil injection. The significant difference of the temperature distribution, depending on oil injection type, highlights the importance of the presented model.

2. Modeling methodology

2.1. Overall description

Fig. 2 shows the 3D computational, bearing-journal domains treated in this study. Fig. 2(a) shows the CFD groove model, where the temperature distribution at the pad leading-edge is utilized to generate the data set for machine learning. Five injection cases are analyzed, in addition to the 3 nozzle, direct lubrication configuration depicted in Fig. 2(a). The CFD groove model includes incompressible, thermal, and transitional turbulence flow, and the momentum equation employs the full Navier-Stokes equation. The rotor-bearing model that excludes the groove regions is illustrated in Fig. 2(b). The rotor-bearing model consists of the shaft, fluid-film, and pad domains.

The generalized Reynolds [3] and energy equation are applied for the fluid-film modeling. The Reynolds equation is derived from the incompressible Navier-Stokes equation by combining the continuity and momentum equations after neglecting the fluid inertia terms with constant pressure assumption in the thin-film (radial) direction. Heat conduction is included for the pad and shaft domains. The pressure and temperature solutions are utilized to predict the thermal-elastic deformation using a structure model. The Reynolds equation reduces computation time significantly when compared to solving the full Navier-Stokes equation, with minimal loss of accuracy. However, the groove region cannot be modeled by the Reynolds equation, due to its non-thin film domain. Therefore, the thermal flow in the groove region is separately simulated by a CFD groove model, and the combination of the CFD groove and rotor-bearing models is implemented via deep (machine) learning for efficient and advanced analysis.

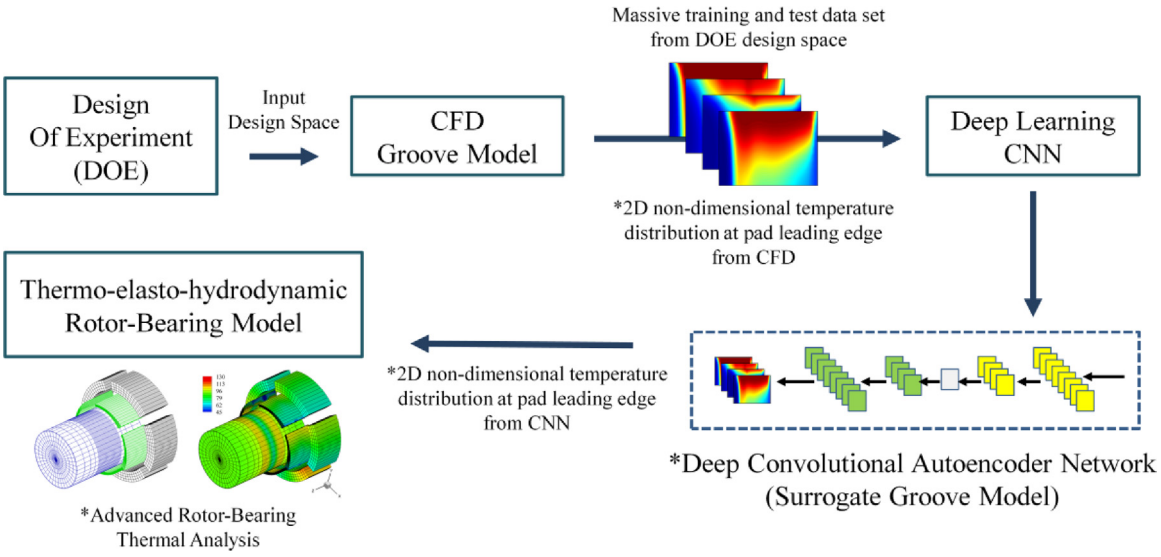

Fig. 3. Illustration of a deep convolutional autoencoder trained by a CFD groove model and its combining with a rotor-bearing model.

Fig. 3 represents the process to combine the groove and rotor-bearing models. The deep convolutional autoencoder neural network has a superior ability with regard to image-to-image prediction [20]. Thus, the CNN, which is one of the deep neural networks, is employed to predict the 2D temperature distribution at the pad leading-edge, while considering the various operating and geometric conditions. Here, the 2D temperature distribution from the neural network is imposed at the pad leading-edge of the fluid-film domain in the rotor-bearing model. The CNN is trained with numerous CFD-generated data sets, through a deep learning algorithm. The neural network needs to provide good performance in the ranges of the designed input parameters (input design space). The input parameters' ranges have been determined based on an exhaustive search of commercial bearing catalogs and based on test cases appearing in the literature [18].

Also, in the input design space, adaptable input parameter combinations need to be generated for composing the training data set. The neural network should achieve reliable generalization in the given input design space, which ensures excellent prediction performance of the neural network for the test data set. The training data set is used during the learning process, whereas the test data set does not participate in the training process. The test data is just utilized for generalization performance verification of the neural network after the training process. Yang and Palazzolo [18] suggested the hybrid Design of Experiment (DOE) with the 2-level full factorial and Latin Hypercube Sampling (LHS) for the input design space, and the DOE yielded the optimal data number and achieved suitable generalization. This DOE method is applied for the input design space in the present study.

2.2. CFD groove model (Data generation)

As illustrated in Fig. 2(a), the oil from the previous pad's trailing-edge (circumferential groove inflow) flows to the next pad's leading-edge (circumferential groove outflow), dragged by the rotating shaft (rotating wall). The liquid oil supplied at the nozzles is discharged to the side outlets (side outflow) with vortex generation inside the groove. The vortex flow mixes the cold supply oil flow and hot circumferential groove inflow. The temperature distribution at the next pad leading edge is mainly affected by a convective mixing process. The flow regime is mainly laminar in the thin-film, but laminar and turbulent flow regimes can coexist in the groove regions, depending on the shaft rotating speed. The turbulent flow is modeled by the Reynolds Averaged Navier Stokes (RANS) equations considering the automatic wall-function and two-equation k-ω based Shear Stress Transport (SST) model [21] for reliable accuracy at low-Reynolds number. The governing equations for the continuity, momentum, turbulent kinetic energy, and turbulent frequency are given in Eqs. (2)-(5), respectively.

Continuity and momentum equations (p', u_i):

$$\frac{\partial \rho_l}{\partial t} + \frac{\partial}{\partial x_i}(\rho_l u_i) = 0 \tag{2}$$

$$\frac{\partial \rho_l u_i}{\partial t} + \frac{\partial}{\partial x_j}\left(\rho_l u_i u_j\right) = -\frac{\partial p'}{\partial x_i} + \frac{\partial}{\partial x_j}\left[\mu_{eff}\left(\frac{\partial u_i}{\partial x_j} + \frac{\partial u_j}{\partial x_i}\right)\right] \tag{3}$$

Turbulent kinetic energy (k):

$$\frac{\partial \rho_l k}{\partial t} + \frac{\partial}{\partial x_j}\left(\rho_l u_j k\right) = \frac{\partial}{\partial x_j}\left[\left(\mu_l + \frac{\mu_t}{\sigma_{k3}}\right)\frac{\partial k}{\partial x_j}\right] + P_k - 0.09\rho_l k\omega \tag{4}$$

Turbulent frequency (ω):

$$\frac{\partial \rho_l \omega}{\partial t} + \frac{\partial}{\partial x_j}\left(\rho_l u_j \omega\right) = \frac{\partial}{\partial x_j}\left[\left(\mu_l + \frac{\mu_t}{\sigma_{\omega 3}}\right)\frac{\partial k}{\partial x_j}\right] + (1-B_1)\rho_l \frac{1.712}{\omega}\frac{\partial k}{\partial x_j}\frac{\partial \omega}{\partial x_j} + \alpha_3 \frac{\omega}{k} P_k - \beta_3 \rho_l \omega^2 \tag{5}$$

The dependent variables of the continuity and momentum equations are the modified pressure (p') and fluid velocity (u_i). ρ_l, μ_l, μ_t, and P_k are the fluid density, fluid dynamic viscosity, eddy viscosity, and turbulent production term, respectively. The summation of the fluid dynamic viscosity and eddy viscosity is the effective viscosity (μ_{eff}). The other constants, including $\sigma_{k3}, \sigma_{\omega 3}, \alpha_3$, and β_3, are determined by the blending function (B_1). Since the transition between laminar and turbulent flow regimes takes place inside the groove, the gamma transitional turbulence model is employed, and the governing equation for the turbulent intermittency, which has zero (laminar) to one value (turbulence), is written in Eq. (6).

Turbulent Intermittency (γ):

$$\frac{\partial \rho_l \gamma}{\partial t} + \frac{\partial (\rho_l u_j \gamma)}{\partial x_j} = \frac{\partial}{\partial x_j}\left[(\mu_l + \mu_t)\frac{\partial \gamma}{\partial x_j}\right] + S_\gamma \tag{6}$$

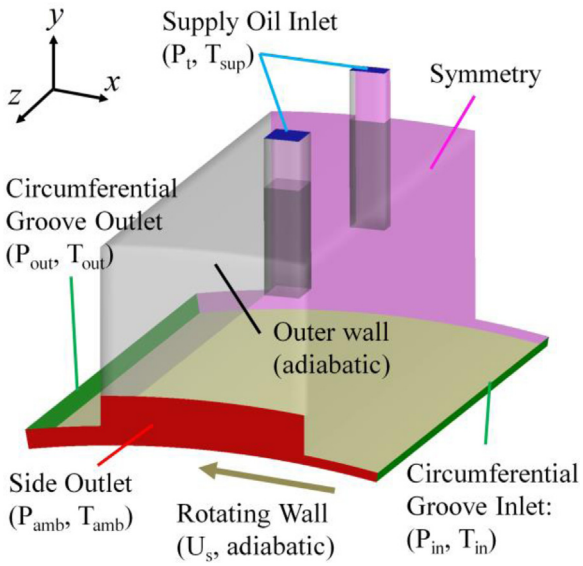

Fig. 4. Boundary conditions for CFD groove model.

The solution of the turbulent intermittency equation modifies the source terms in Eq. (4) to reflect the effect according to the flow regimes. The source term (S_γ) of Eq. (6) mainly depends on the transition onset Reynolds number. In addition, the fluid energy equation expressed in Eq. (7) is solved to get the temperature field for the groove model.

Fluid Energy Equation (T_l):

$$\frac{\partial \rho_l h_{tot}}{\partial t} - \frac{\partial p}{\partial t} + \frac{\partial}{\partial x_j}\left(\rho_l u_j h_{tot}\right) = \frac{\partial}{\partial x_j}\left(\lambda_l \frac{\partial T_l}{\partial x_j}\right) + \frac{\partial}{\partial x_j}\left[u_i\left(-p'\delta_{ij} + \mu_{eff}\left(\frac{\partial u_i}{\partial x_j} + \frac{\partial u_j}{\partial x_i}\right)\right)\right] \quad (7)$$

p, h_{tot}, and λ_l are the static pressure, total enthalpy, and fluid thermal conductivity.

Fig. 4 shows the boundary conditions for the CFD groove model. The circumferential groove inlet and outlet and side outlets are prescribed with the static pressure, temperature, and zero gradient turbulence. The total pressure, temperature, and medium turbulence intensity are imposed at the supply oil inlet. The moving wall boundary condition is applied at the journal surface to account for the shaft rotation effect. All wall boundary conditions are assumed adiabatic due to the dominant influence of advection heat. Only the symmetric half domain with respect to the x-y plane is considered, in order to reduce computational load.

ANSYS CFX is utilized as the CFD solver. The high-resolution advection scheme is selected in the CFD solver. The CFD solver obtains the solution for the dependent variables in the transient analysis (Second Order Backward Euler). The initial condition, time step, and duration are suitably determined to guarantee robust convergence from the empirically acquired information based on numerous simulations. Also, mesh density is reasonably applied through an adaptable grid study. Fig. 5(a) illustrates a mesh independence result, for a representative set of model parameters. The mesh density (Fig. 5(b)), with 30,789 elements, is adopted to obtain both accuracy and computational efficiency. This was accomplished by verification with a full CFD model [10,12]. The 30,789 element mesh is implemented for all oil injection cases.

To generate the massive training and test data for machine learning, automatic geometry generation, meshing, solving, and data-saving methods have been established by a developed Python code compatible with the ANSYS workbench environment. The computations are parallelly executed by the supercomputing system (Texas A&M University High Performance Research Computing, TAMU HPRC).

2.3. Deep convolutional autoencoder (Surrogate groove model)

The main benefit of applying machine learning, instead of the direct combination of the groove CFD model with the dynamic rotor-bearing model, is to reduce the calculation time significantly. The artificial neural network needs to predict the 2D temperature distribution at the circumferential groove outlet, and it can be classified as the image regression in machine learning. The CNN has a strong ability when conducting image classification and recognition in machine learning [20]. Furthermore, from a comparative study on shallow, deep feed-forward, and deep CNNs, the superiority of the CNN has been confirmed as a surrogate groove model when viewing the computational time and the regression performance. Thus, the convolutional autoencoder network is chosen in this research for the image (2D temperature distribution) prediction.

A complex neural network may cause an overfitting problem (significant test data error) with increased training time. In contrast, a simple neural network can have difficulty getting reliable neural network performance. So, an optimal neural network is searched by adjusting neural network size until the test data error reaches a minimized value. The designed neural network is illustrated in Fig. 6. The input image of the CNN is encoded and then decoded to reconstruct the image via the filters (or kernels) of

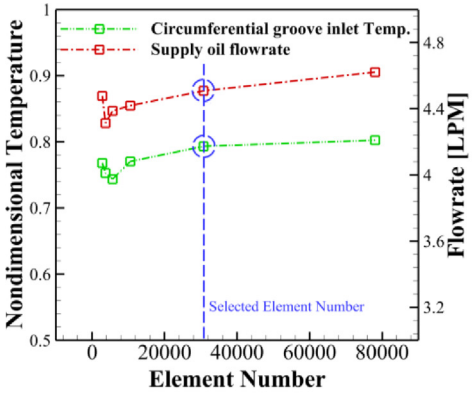

(a)

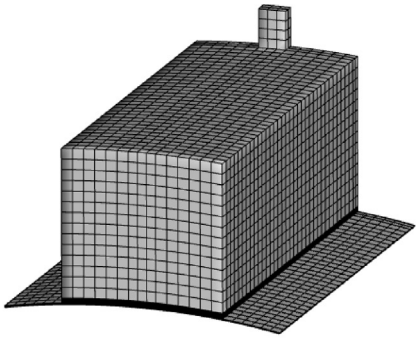

(b)

Fig. 5. (a) Mesh independence results and (b) typical groove mesh. Groove geometry is for a 101.6 mm diameter, 50.8 mm length, 5 pads, 60 deg pad arc length bearing.

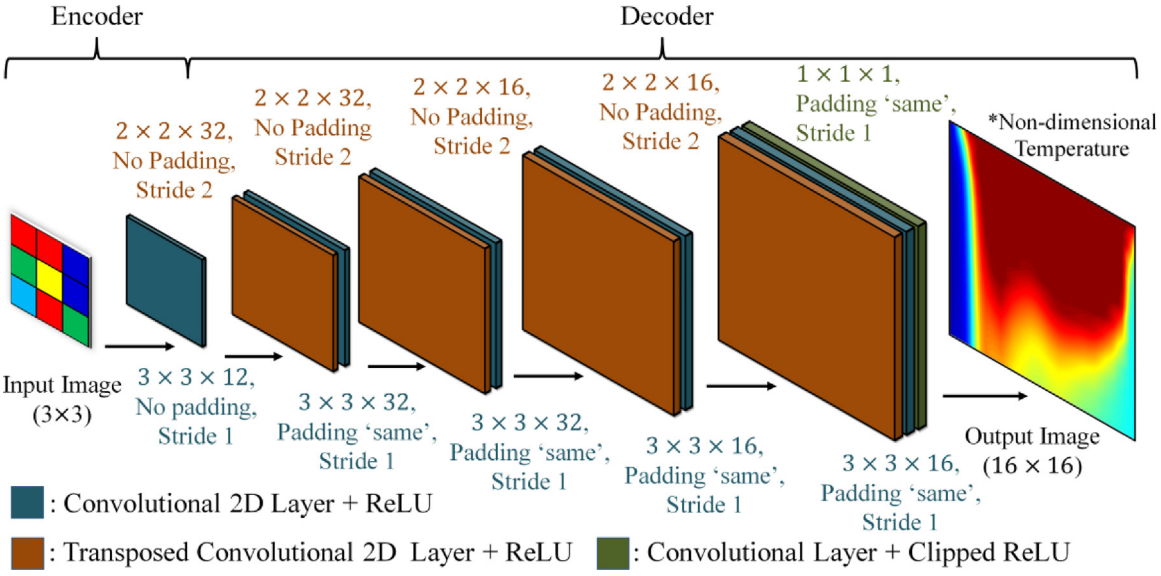

Fig. 6. Designed convolutional autoencoder neural network.

the convolutional layer, which can perceive various patterns (edges, corners, etc.). The input image (3 by 3 matrix) is made by nine input parameters (numeric values) that are transformed from zero to one, and the input parameters are specified in Section 3.1. The encoder has only a 2D convolutional layer regarding the small size of the input layer, and the decoder is comprised of the transposed convolutional and convolutional layers to generate the output image (16 by 16 matrix) which represents the non-dimensional temperature distribution at the circumferential groove outlet. The output values are limited to zero to one by the clipped ReLU (Rectified Linear Unit).

The convolutional layer convolves the input through the shift of kernel in the vertical and horizontal direction with two strides (two pixels) while calculating the dot product of weight factors and input and then adding the bias factor. The transposed convolutional layer expands input size by leaving a space between the input elements with two strides. The other calculation procedure is analogous to the non-transposed convolutional layer. Fig. 7 depicts the convolution (Fig. 7(a)) and transposed convolution (Fig. 7(b)) steps of the input, via the kernel shift with numeric examples.

The ReLU ($f(x) = \max[0, x]$), which is an activation function, is followed by the transposed and non-transposed convolutional layers. The padding is utilized to adjust the output size, and the same padding makes the output size have the same size as the input size. The pooling layer is not considered because an apparent benefit was not observed in this study.

The Adam algorithm (adaptive momentum estimation) is applied, with sampling a minibatch and shuffling every epoch, for neural network training, which is the process to find the weighting and bias factors through an optimization algorithm. The training computation is carried out by taking advantage of the power of GPU (Graphics Processing Unit), and it is implemented by MATLAB. The minibatch size, learning rate, L2 regularization factor, gradient decay factor, and squared gradient decay factor are 128, 1.e-3, 1.e-4, 0.9, and 0.999.

2.4. Rotor-bearing model

The computational domains for the rotor-bearing model are depicted in Fig. 2(b), and the domains include the fluid-film, rotor, and bearing (five pads). As mentioned in Section 2.1, the fluid-film is simulated by the generalized Reynolds equation in the following

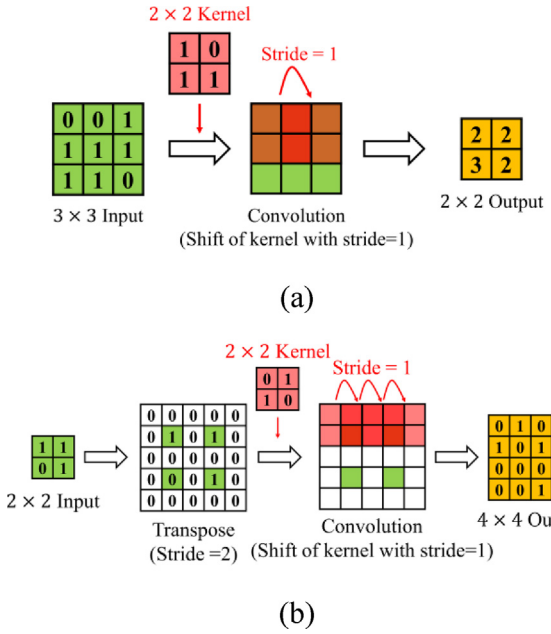

Fig. 7. Examples of (a) convolution and (b) transposed convolution steps.

equation.

$$\nabla \cdot (D_1 \nabla p) + (\nabla D_2) \cdot U_s + \frac{\partial h_l}{\partial t} = 0 \tag{8}$$

p is the static pressure (dependent variable), and U_s is the shaft surface velocity. D_1 and D_2 are given in the following equations respectively.

$$D_1 = \int_0^{h_l} \int_0^z \frac{\xi}{\mu_l} d\xi dz - \int_0^{h_l} \frac{\xi}{\mu_l} d\xi \int_0^{h_l} \int_0^z \frac{1}{\mu_l} d\xi dz / \int_0^{h_l} \frac{1}{\mu_l} d\xi \tag{9}$$

$$D_2 = \int_0^{h_l} \int_0^z \frac{1}{\mu_l} d\xi dz / \int_0^{h_l} \frac{1}{\mu_l} d\xi \tag{10}$$

The film thickness (h_l) is expressed by

$$h_l = \sqrt{(x_p - x_R)^2 + (y_p - y_R)^2} - R_s - h_{te} \tag{11}$$

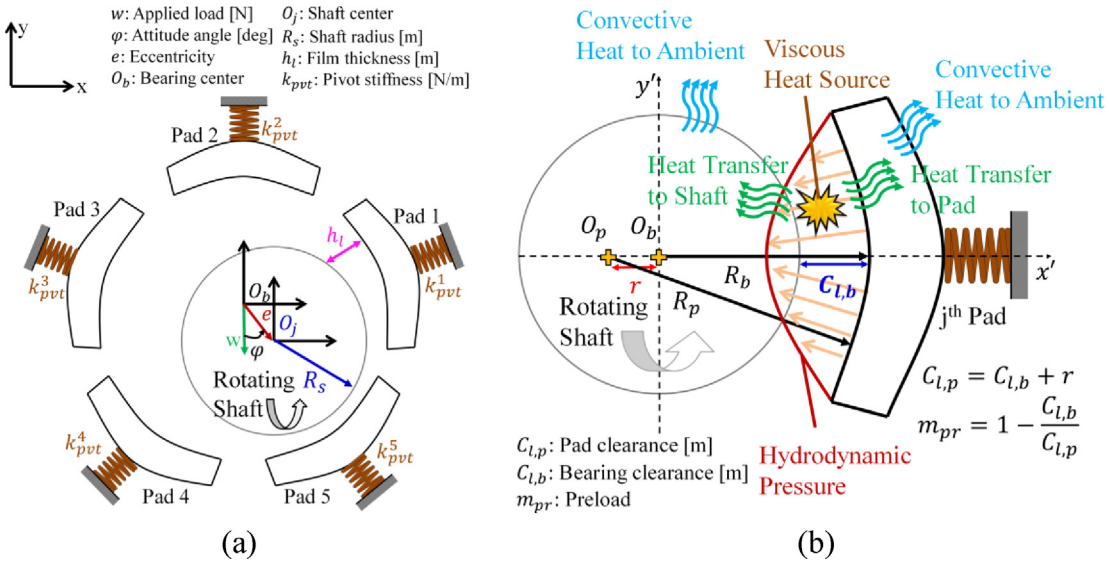

Fig. 8. Illustrations of geometric parameters and heat transfer mechanism in rotor-bearing system; (a) geometric parameters over entire bearing, (b) heat transfer mechanism with geometric parameters.

where x_p and y_p are the pad x and y coordinates at the interface between the fluid-film and pad, and x_s, y_s, R_s, and h_{te} are the shaft x-displacement, shaft y-displacement, shaft radius, and film thickness change from shaft and pad thermal expansions [3]. The fluid dynamic viscosity is ($\mu_l = \mu_o e^{\alpha(T_l - T_o)}$, where μ_o: viscosity at reference temperature, T_o: reference temperature, α: decay constant). Since the viscosity varies with fluid temperature, the Reynolds equation is considerably influenced by the solution of the energy equation

$$\rho_l c_{p,l}\left(\frac{\partial T_l}{\partial t} + \vec{U}\cdot\nabla T_l\right) = \nabla\cdot(\lambda_l \nabla T_l) + \mu_l\left[\left(\frac{\partial u}{\partial y}\right)^2 + \left(\frac{\partial w}{\partial y}\right)^2\right] \tag{12}$$

where $c_{p,l}, \lambda_l$, and $\vec{U}$ are the fluid specific heat, thermal conductivity, and velocity vector, respectively. The velocity field (u, v, w) is derived from the pressure field [3]. The thermal deformation of the solid domains by the temperature, impacts the film thickness which is a sensitive parameter in the Reynolds equation, and so the temperature prediction for the solid domains should be considered. The heat conduction equation for the solid domain is

$$\rho_s c_{p,s}\frac{\partial T_s}{\partial t} = \nabla\cdot(\lambda_s \nabla T_s) \tag{13}$$

ρ_s, $c_{p,s}$, λ_s, and T_s are the solid density, specific heat, thermal conductivity, and temperature with respect to the shaft and pads. In addition, the thermal elastic deformation of the solid domains is calculated with a 3D structure model [10].

The Reynolds equation requires the pressure boundary conditions at the pad leading and trailing edges and the side outlets. The ambient pressure (static) is imposed at the side outlets, and the pressure of the pad leading and trailing edges are determined from the surrogate groove model between pads [18]. For the thermal boundary conditions, the temperature at the pad leading-edge is prescribed by the trained CNN, and zero gradient temperature is applied at the pad trailing edge and side outlets. The interface boundaries between the shaft and fluid-film and between the fluid-film and pad are set up to maintain the temperature and heat flux continuity. The outer surfaces of the shaft and pads are prescribed by heat transfer coefficient and ambient temperature. The boundary conditions for the structure model are well specified in the previous study [10], and this study suitably adopts identical way to consider the pivot stiffness depicted in Fig. 8(a).

Fig. 8 represents the important geometric parameters used in this study and the major heat transfer mechanism. The second term of the right-hand side of Eq. (12) is the main heat source by viscous dissipation, and the generated heat in the thin-film is transported in the circumferential direction and diffused to the ambient passing through the rotating shaft and pads. Here, the 2D temperature distribution at the pad leading-edge of the fluid-film is significant since it directly affects the amount of heat transferred to the shaft and pad, solid temperature distribution, and solid thermal deformation. It highlights the importance of the proposed surrogate groove model, considering the 2D temperature distribution at the pad leading-edge. In order to solve the governing equations with discretization, the Finite Volume Method (FVM) is employed for the fluid-film domain, and the Finite Element Method (FEM) is applied for the structure model. The computation is implemented by in-house-based MATLAB/C/C++ code.

2.5. Calculation procedure

For the rotor and pad degrees of freedom, a dynamic structure model with modal reduction technique is employed to eliminate the singularity problem with a static structure model [3]. Fig. 11 represents the calculation procedure for static performance and dynamic coefficient prediction of a tilting pad journal bearing. Time integration is performed for the structure model utilizing the adaptive Runge-Kutta method. During the time integration, the Reynolds and energy equations in the fluid-film have been sequentially solved while updating the temperature distribution at the pad leading-edges by the trained CNN. In addition, the film thickness and its time derivative changes with time due to the displacement and velocity of the rotor and pads. The Reynolds and energy equations are coupled through the dynamic viscosity and fluid velocity. The Reynolds model yields the pressure solution to derive the fluid velocity, and the fluid velocity is transferred to the energy equation of the fluid film. The energy equation updates the dynamic viscosity in the Reynolds equation by utilizing the new fluid velocity and temperature. The dynamic viscosity varies only with temperature and the density is a constant. The pressure and temperature solutions are applied to the interface boundary conditions of the solid domains, after reaching the equilibrium state of

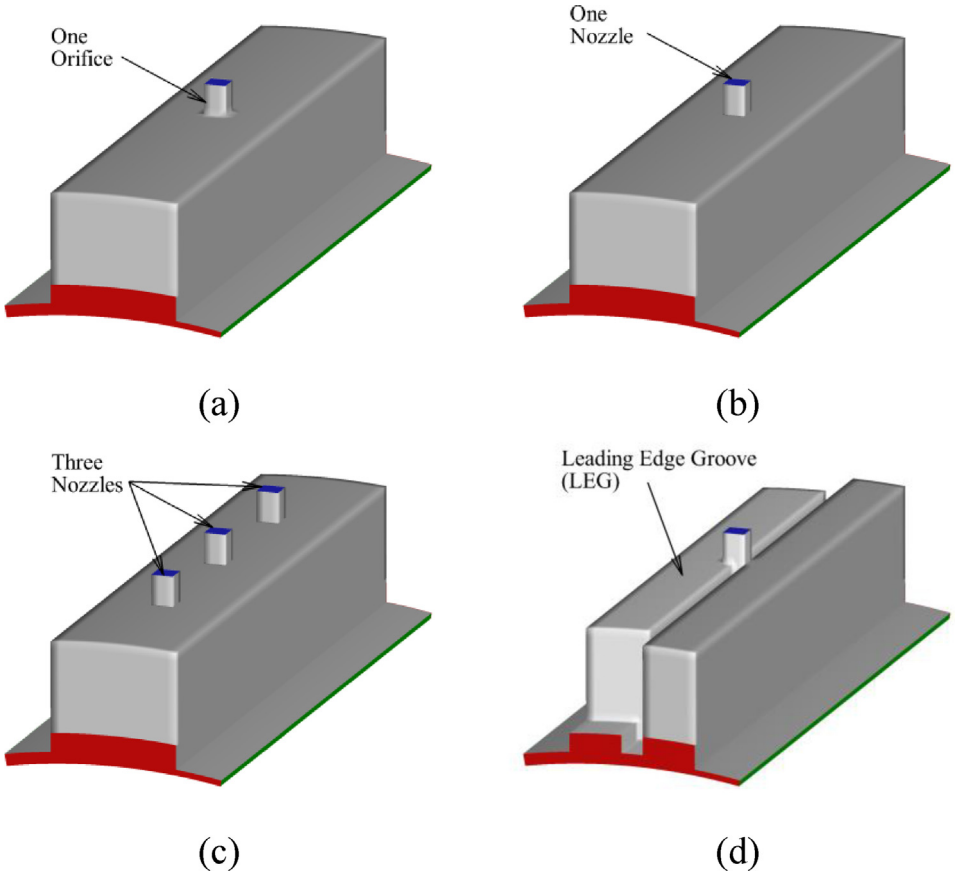

Fig. 9. Various types of oil injection treated in this study; (a) one orifice, (b) one nozzle, (c) three nozzles, (d) leading edge groove (LEG).

the rotor and pads. Then, the temperature of the solid domains is obtained by solving the heat conduction equation. The solid temperature solution is input in the thermal deformation solver, with displacement solution transferred to the fluid-film model for the interface boundary prescription. The thermal deformation changes the film thickness in the Reynolds equation. The calculation procedures above continue until the relative error of the temperature of all domains reaches the given criteria.

3. Results and discussion

3.1. Case description and dataset

This section explains the cases according to various oil injection types, and their generated datasets from the CFD groove model. Lubrication can be classified as either flooded or direct lubrication. The flooded lubrication is the conventional one, and it has an orifice with close-end seals (relatively larger diameter and thin seal height). On the contrary, the direct lubrication has one or multiple nozzles with open-end seals (relatively smaller diameter and thick seal height). Fig. 10(a) shows the orifice diameter (D_g) and seal height (h_s). The direct lubrication has an exceptional cooling ability (low temperature) at the pad leading-edge of the fluid film, contrary to the flooded lubrication. This cooling capability is implemented by small diameter nozzles and open-end seals. The nozzles help penetrate the supplied oil to the shaft surface with less pressure drop by the open-end seals. Also, mixed lubrication is utilized, which can be made from the combination of direct and flooded lubrication features.

Fig. 9 shows the four lubrication types treated in this study, and Fig. 10 illustrates the lubrication types with the design parameters and transparency for better understanding. The following specifies the five cases referring to the lubrication geometries in Fig. 10.

(1) Case 1: small 1 orifice, closed-end seal, mixed lubrication, depicted in Fig. 10(a)
(2) Case 2: large 1 orifice, closed-end seal, flooded lubrication, depicted in Fig. 10(a)
(3) Case 3: 1 nozzle, open-end seal, direct lubrication, depicted in Fig. 10(b)
(4) Case 4: 3 nozzles, open-end seal, direct lubrication, depicted in Fig. 10(c)
(5) Case 5: LEG, closed-end seal, mixed lubrication, depicted in Fig. 10(d)

Table 1 shows that the open-end condition has a seal height (h_s) approximately an order of magnitude larger than the close-end condition. The seal height values divided by the shaft radius (R_s) are provided for all oil injection types. Figs. 9 and 10 show highly magnified depictions of the seal heights for better visualization.

The CNNs are trained for the five oil injection cases to investigate the groove thermal mixing effect and its heat transfer effect in the rotor-bearing system when the surrogate groove model is combined with the rotor-bearing model. Table 1 summarizes the input parameters and dataset numbers for the various oil injection cases. The nine (9) parameters used as the neural network input in Table 1 are selected from the parameter's sensitivity analysis [18], and the parameters are depicted in Fig. 10(a). The neural network input ranges are determined based on the frequency of use in actual practical applications [18]. For each oil injection case, the input space is designed by the combination of the Full Factorial and Latin Hypercube Sampling methods for the 1536 training data set generation, and the 658 test data sets with randomly extracted in-

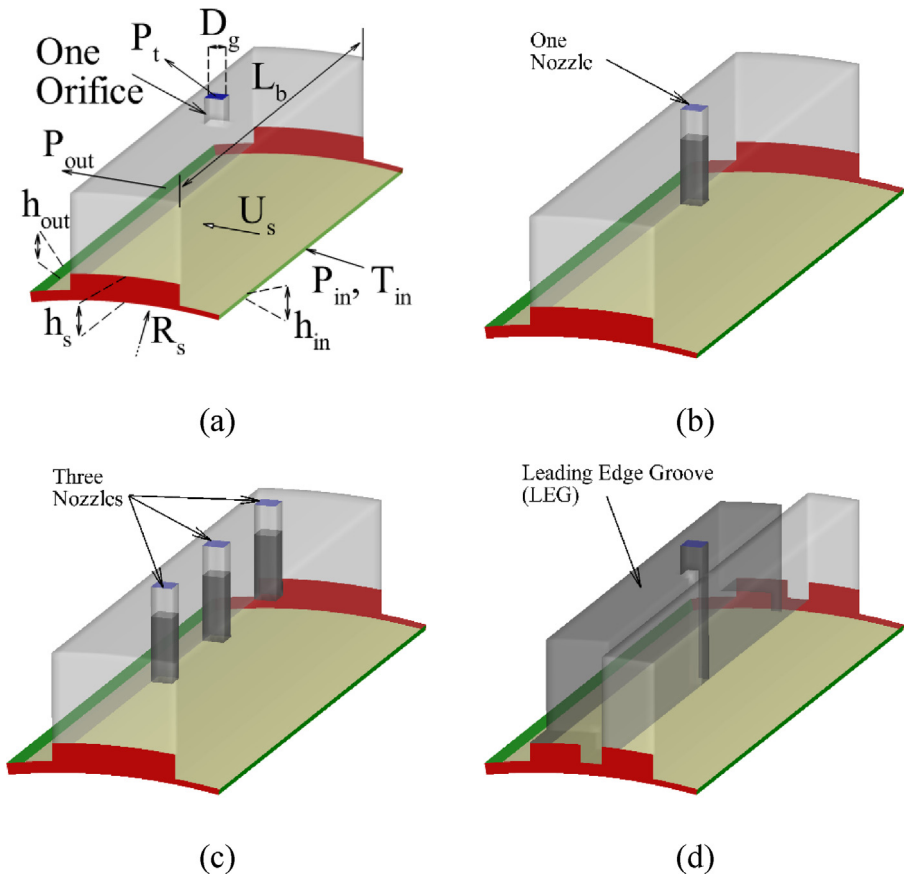

Fig. 10. Various types of oil injection with input parameters and transparency; (a) one orifice with input parameters, (b) one nozzle, (c) three nozzles, (d) leading edge groove (LEG); *D_g: nozzle or orifice diameter [m], P_t: total pressure [Pa], L_b: bearing length [m], U_s: shaft surface velocity [m/s], P_{in}: groove inlet pressure [Pa], T_{in}: groove inlet temperature [C], h_{in}: groove inlet height [m], P_{out}: groove outlet pressure [Pa], h_{out}: groove outlet height [m], R_s: shaft radius [m], h_s: seal height [m].

Table 1
Input parameter, data set number, performance on designed convolutional autoencoder neural networks.

Oil Injection Type	Case 1	Case 2	Case 3	Case 4	Case 5
Oil Injection Number	1	1	3	1	1
Direct or Flooded?	Mixed	Flooded	Direct	Direct	Mixed
Constant Input Parameters					
D_g/W_g	0.169	0.357	0.282	0.171	0.160
h_s/R_s	0.0084	0.0063	0.0500	0.0500	0.0049
$C_{l,b}/R_s$	0.0015	0.0015	0.0015	0.0015	0.0016
Neural Network Input Parameters and its Range					
R_s [mm]	25.4–76.2				
L_b/R_s	0.4–1.0				
U_s [m/s]	15–95				
P_t [MPag]	0.01–0.7				
P_{in} [MPag]	0–1.2				
P_{out} [MPag]	0–0.65				
$h_{in}/C_{l,b}$	0.3–2.2				
$h_{out}/C_{l,b}$	0.3–2.2				
T_{in} [C]	50–120				
CFD Image Data Number in Designed Input Space					
Training Data (FF)	512	512	512	512	512
Training Data (LHS)	1024	1024	1024	1024	1024
Test Data (Random)	658	658	658	658	658
Total Data	2194	2194	2194	2194	2194
Performance of Trained CNN					
R-squared (train data)	0.995	0.997	0.996	0.997	0.996
RMSE (train data)	0.0252	0.0226	0.0203	0.0185	0.0253
R-squared (test data)	0.987	0.988	0.985	0.992	0.984
RMSE (test data)	0.0406	0.0427	0.0393	0.0293	0.0462

*FF: Full Factorial (2 level), LHS: Latin Hypercube Sampling, W_g: groove width, RMSE: Root Mean Squared Error

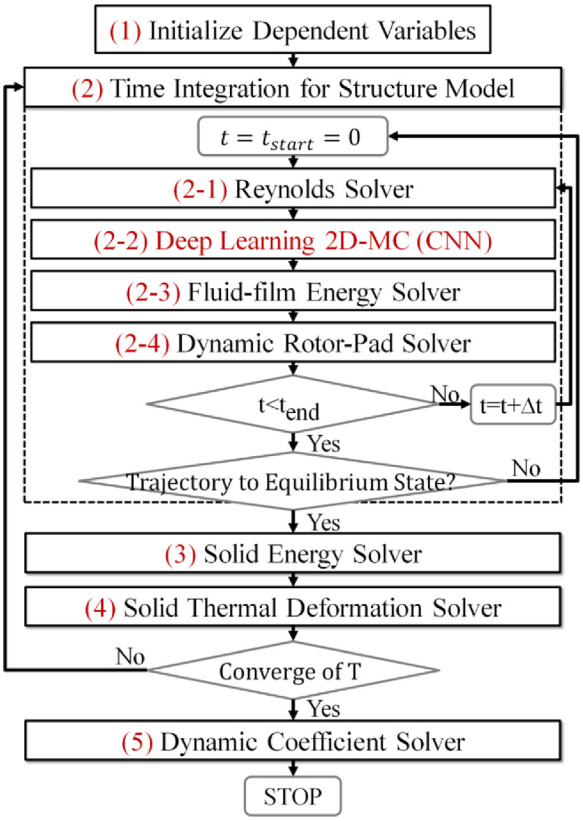

Fig. 11. Calculation procedure for static performance and dynamic coefficient prediction of a tilting pad journal bearing.

put combinations are produced for the validation and generalization check of the trained neural network.

3.2. Deep convolutional autoencoder performance

The performance of the trained CNN can be estimated by the R-squared and Root Mean Squared Error (RMSE) for the regression. Table 1 shows that the CNN of all cases shows the excellent regression performance, which has the R-squared value near one and a low RMSE for both training and test data set. The CNN needs to have good generalization ability without an overfitting problem. The test dataset does not participate in the training process, and the test dataset can be commonly used to check the generalization status of the trained CNN. Thus, the non-dimensional temperature distributions at the pad leading edge of the fluid-film are compared for the CFD and CNN predictions, using the randomly extracted test data, as shown in Figs. 12-16. The non-dimensional temperature is defined in Eq. (1). Fig. 12(a) shows the representative 2D temperature distribution with the one oil injection, and it is drawn to describe the information needed in the contours represented in Figs. 12-16. The half-symmetric temperature contour with respect to the x-y plane is plotted, since the symmetry boundary condition is applied for the CFD groove model. The top and bottom horizontal edges are the shaft and pad surfaces at the pad leading edge of the fluid film, respectively. The right vertical edge indicates the side outlet. The value near one (red) means that the fluid is not cooled when passing through the groove region, and the zero value (blue) represents the strong mixing with the cooled supply oil.

Fig. 12(a) shows that the oil near the supply oil inlet is penetrated to the shaft surface with the strong cooling of the hot oil transported from the circumferential groove inlet. Also, it is confirmed that the oil temperature is decreased near the side outlet. This is because some portion of the flow from the supply oil inlet is discharged to the side outlet while mixing with the hot oil. The temperature in the region between the oil injection and side outlet of the temperature contour is mainly affected by the ratio of the groove circumferential inlet film thickness to the groove circumferential outlet film thickness, since there is no penetrating flow and the heat is transported by the circumferential heat advection term with negligible conduction effect.

The non-dimensional temperature distribution predicted in the groove model with one nozzle injection shows a similar temperature distribution pattern, as represented in Figs. 12, 13, 14, and 16. In the case of three nozzles, the additional oil penetration region is generated, as shown in Fig. 15. It is interesting to compare the flooded lubrication in Fig. 13 and direct lubrication in Figs. 14 and 15. It is apparent that the oil penetration in the direct lubrication is stronger than that in the flooded lubrication, and this gives the better cooling ability in the direct lubrication, as mentioned earlier. Also, suppose the orifice or nozzle size is small enough despite equipping with the close-end seals such as Case 1 (Fig. 12) and Case 5 (Fig. 16). In that case, it is confirmed that the intense oil penetration can be generated due to its higher dynamic pressure at the supply oil inlet.

As seen in Figs. 12-16, the non-dimensional temperature distribution is distinctly different according to the input parameters as illustrated in Fig. 10(a), and it stresses the importance of considering the 2D, pad inlet temperature distribution. In addition, the deep convolutional autoencoder neural network predicts the temperature distribution accurately when compared to the CFD predictions, as shown in Figs. 12-16. These are very intriguing results because the CNN shows excellent performance for the test data, proving its ability as the surrogate model and the generalization capability. In addition, the CNN calculates the non-dimensional temperature distribution at the pad leading-edge of the fluid film within 1.e-6 s, which is 9 orders of magnitude faster than the CFD computation which takes around 1–2 h. This enables the practical implementation of the CNN as a sub-model in the overall dynamic rotor-bearing model, yielding significant increase in model accuracy, with little increase in computation time.

3.3. Model validation

The trained CNN is combined with the rotor-bearing model to investigate the 2D temperature distribution effect at the pad leading-edge, and the validity of the proposed model is verified in this section. The groove region is modeled by the CNN trained based on CFD data, and the fluid film on the pad regions is simulated through the Reynolds equation. The Reynolds model though simplified, is highly accurate for thin-film modeling, as confirmed by comparing with full CFD model results. Yang and Palazzolo [10–12] developed the full CFD model for a rotor-bearing system, and the input parameters and results in the study are used for the validation. The specific input parameter values are given in Table 2, and Fig. 8 illustrates these geometric parameters. The lubrication type is identical to Case 1 represented in Section 3.1, and so the CNN for Case 1 is applied in the proposed model. The number of elements in the computational domain, as depicted in Fig. 2(b), is 45,920, and is selected based on a thorough grid test.

A Reynolds-based model is used to compare results obtained with the groove model developed by Suh et al. [3] or Abdollahi et al. [4], the proposed (deep learning groove mixing) model and the full CFD model. The method suggested by Abdollahi et al. [4], requires the supply oil flow rate as an input, so an identical supply flow rate is applied in the CFD simulations.

Fig. 17 compares results for static and dynamic bearing parameters, utilizing the various modeling approaches. The eccentricity ratio is defined by $e/C_{l,b}$, which is a measure of shaft displacement

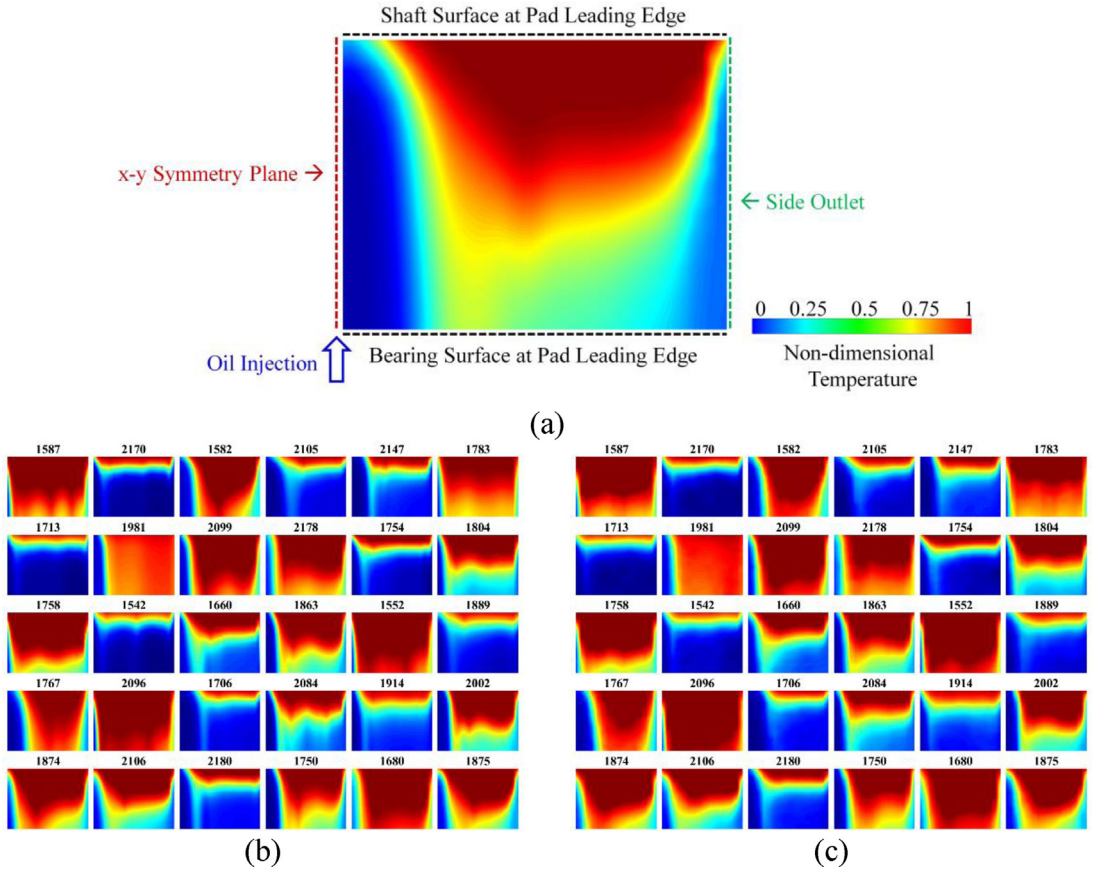

Fig. 12. Prediction of non-dimensional temperature distribution at pad leading edge – randomly extracted test data (No. 1537 - 2194) comparison for small 1 orifice, close-end seal (Case 1); (a) figure structure description, (b) CFD, (c) deep convolutional autoencoder (CNN).

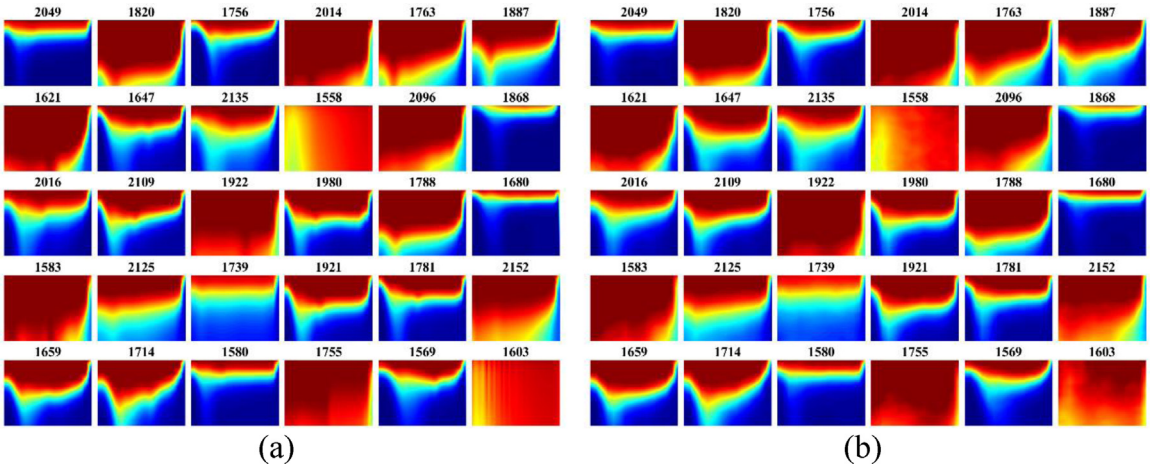

Fig. 13. Prediction of non-dimensional temperature distribution at pad leading edge – randomly extracted test data (No. 1537 - 2194) comparison; (a) CFD, (b) deep convolutional autoencoder (CNN); large 1 orifice, close-end seal (Case 2).

due to the static applied load (w), where eccentricity (e), and bearing clearance ($C_{l,b}$) are represented in Fig. 8. The dynamic coefficients, including the stiffness and damping coefficients, are used to evaluate the stability and critical speeds of a rotor-bearing model, and the method to calculate the dynamic coefficients is presented in previous studies [10–11].

The results in Fig. 17(b)-(e) demonstrates that conventional approaches, employing groove mixing parameters (mixing coefficient or groove efficiency parameter), may yield a wide range of predicted static or dynamic parameter values depending on the assumed values of these parameters. This uncertainty lessens the reliability of these approaches. In contrast, the groove model utilizing deep learning does not require assuming a value for a groove mixing parameter. Furthermore, the proposed model, which combines the Reynolds approach with the deep learning groove mixing model, has excellent agreement with full CFD models, confirming the model's reliability via simulation studies. The results of this approach are further presented in Section 3.4.

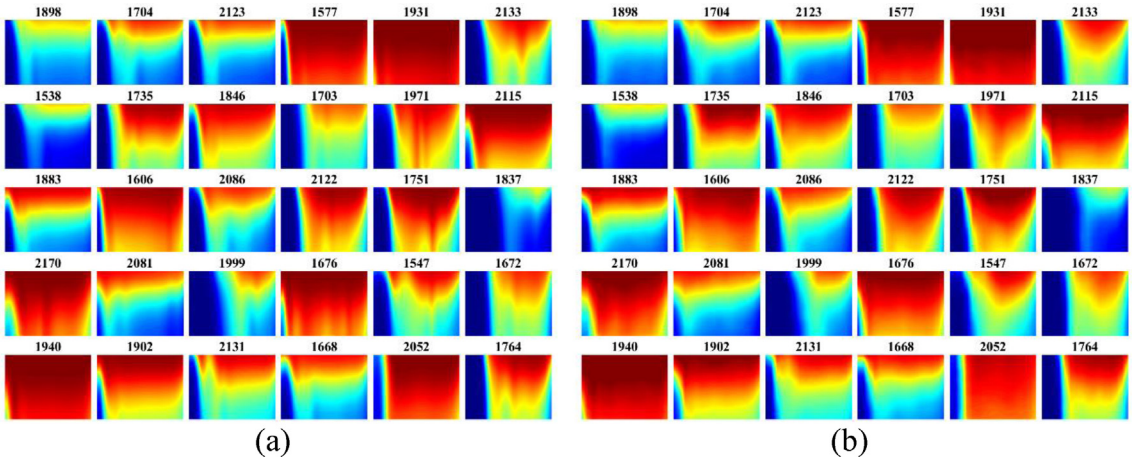

Fig. 14. Prediction of non-dimensional temperature distribution at pad leading edge – randomly extracted test data (No. 1537–2194) comparison; (a) CFD, (b) deep convolutional autoencoder (CNN); 1 nozzle, open-end seal (Case 3).

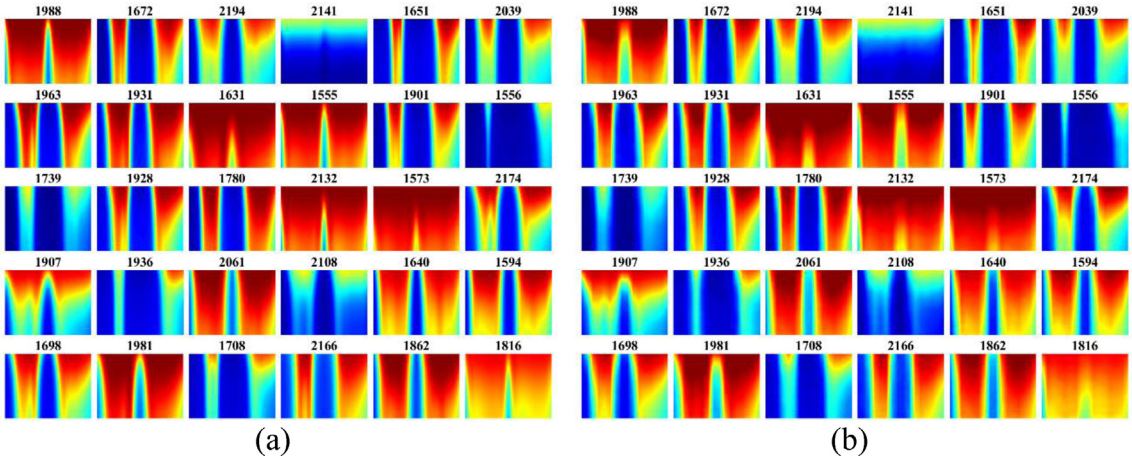

Fig. 15. Prediction of non-dimensional temperature distribution at pad leading edge – randomly extracted test data (No. 1537–2194) comparison; (a) CFD, (b) deep convolutional autoencoder (CNN); 3 nozzles, open seal (Case 4).

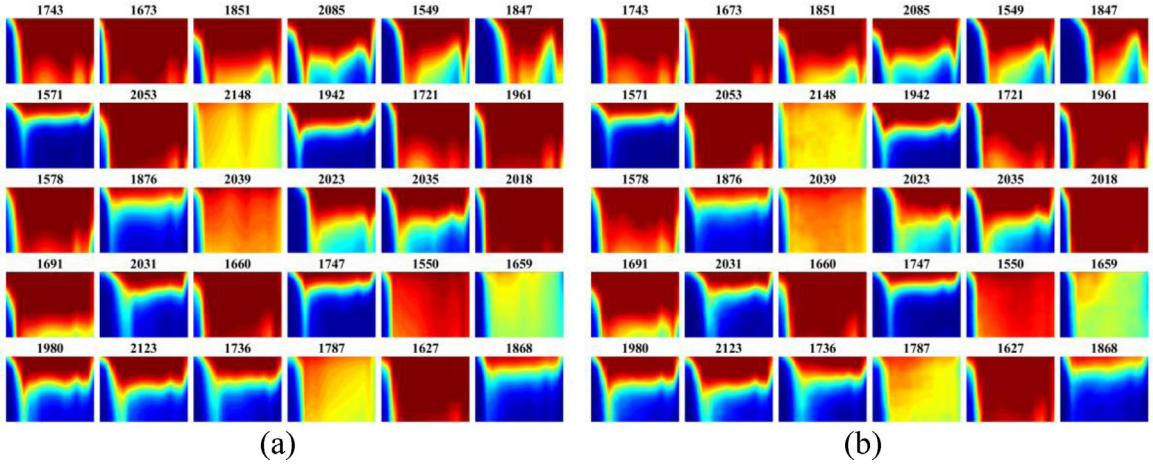

Fig. 16. Prediction of non-dimensional temperature distribution at pad leading edge – randomly extracted test data (No. 1537–2194) comparison; (a) CFD, (b) deep convolutional autoencoder (CNN); LEG, closed seal (Case 5).

The proposed model is compared with the test data in [19] for experimental validation. The test was conducted for a tilting pad journal bearing with the LEG (Leading Edge Groove) lubrication type, identical to Case 5 described in Section 3.1. The bearing has five pads, and the shaft diameter and bearing length are 101.587 mm and 60.325 mm, respectively. The other input parameter values are provided in the prior study [12]. As shown in Fig. 18, the eccentricity ratio, bottom pad trailing edge temperature, and dynamic coefficients are compared between the proposed model and test data. The results pre-

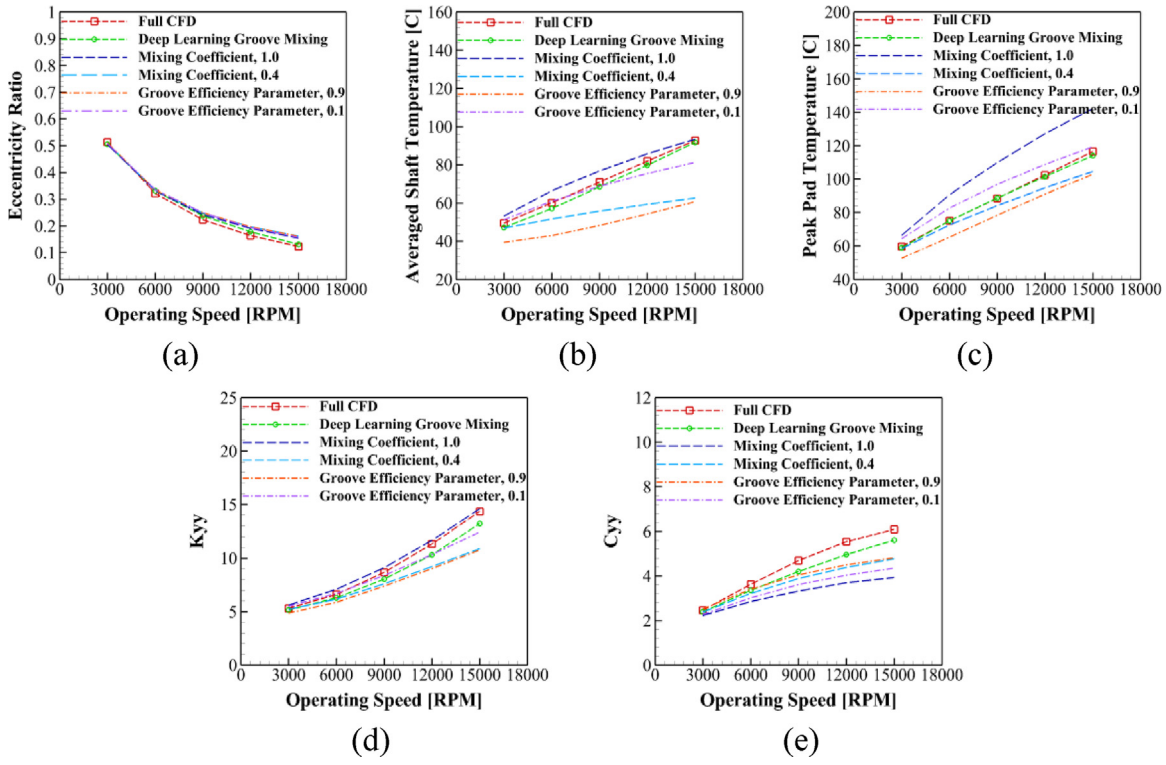

Fig. 17. Comparison between full CFD [18] and Reynolds approaches; (a) eccentricity ratio, (b) averaged shaft temperature, (c) peak pad temperature at mid-span, (d) non-dimensional stiffness (K_{yy}), (e) non-dimensional damping coefficient (C_{yy}).

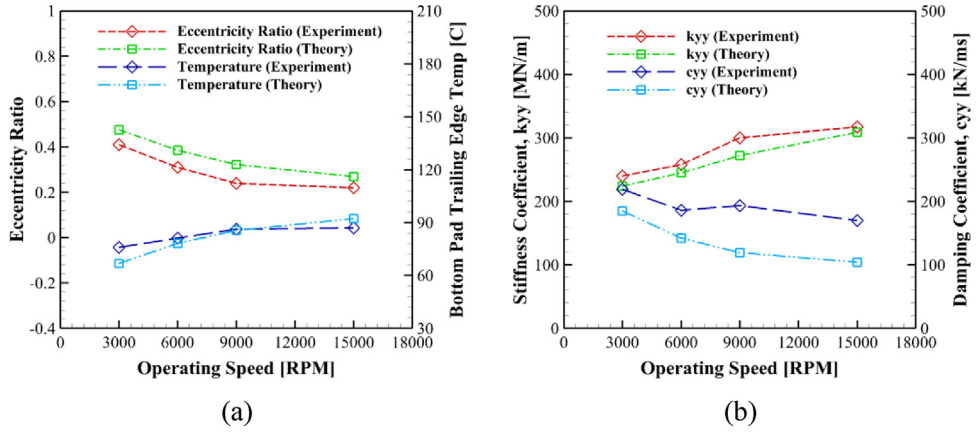

Fig. 18. Comparison between experiment and the proposed theoretical model; (a) eccentricity ratio and bottom pad trailing edge temperature, (b) stiffness (k_{yy}) and damping (c_{yy}) coefficients.

dicted by the proposed model agree well with the experimental data.

3.4. Thermal analysis of rotor-bearing model

This section provides thermal analysis results of the rotor-bearing system for the various oil injection types (Case 1 – Case 5) and supply oil flow rate (35 LPM, 52.5 LPM) when applying the Reynolds-based rotor-bearing model combined with the surrogate groove model. The input parameters are identical for all cases, as provided in Table 2. The total supply pressure in the CNN is determined iteratively to obtain the desired supply oil flow rate [18]. Fig. 19 shows the comparison results for the various oil injection types.

The eccentricity ratio decrease confirms the lift of the shaft with increased operating speed, due to the strengthened converging wedge effect in the thin-film, as shown in Fig. 19(1). The eccentricity ratio is nearly insensitive to the oil injection lubrication types. Accurate prediction of temperature is imperative. For example, the babbitt surface on the bearing can typically only endure temperatures below 120 [C], and the rapid increase or circumferential difference of shaft temperature can induce rotor vibration instability. Fig. 19(2) and (3) confirm that shaft and pad temperatures are highly sensitive to the various oil injection types. Therefore, usage of the proposed CNN groove model is important, since conventional mixing parameter models may yield widely varying predictions depending on the parameter values that are assumed.

The shaft and pad temperatures increase with operating speed due to the higher viscous heat generation. From the averaged shaft and peak pad temperature results in Fig. 19(2) and (3), the direct lubrication with open-end seals shows the best cooling ability for the shaft and pads. In contrast, the oil injection types with close-

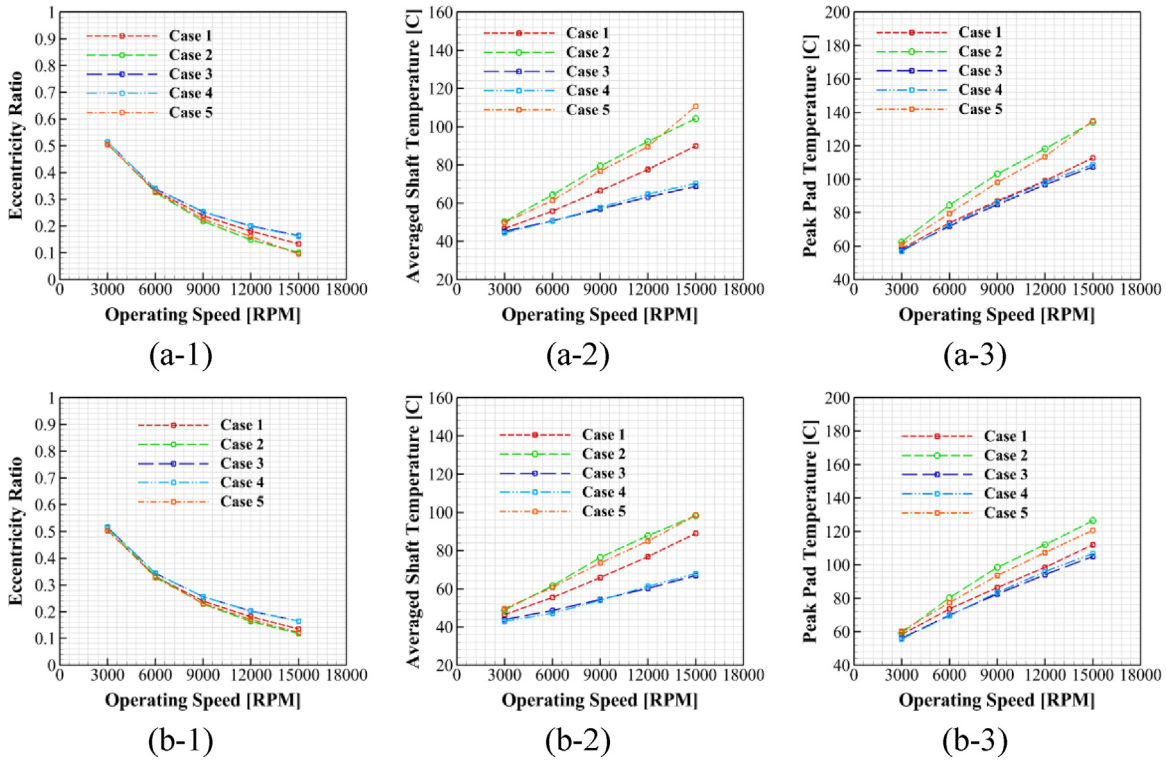

Fig. 19. Eccentricity ratio and averaged shaft temperature for various injection types; (a) 35 LPM, (b) 52.5 LPM; (1) eccentricity ratio, (2) averaged shaft temperature [C], (3) peak pad temperature at mid-span [C]; Case 1: small 1 orifice-closed seal, Case 2: large 1 orifice-closed seal, Case 3: 1 nozzle-open seal, Case 4: 3 nozzles-open seal, Case 5: LEG-closed seal.

Table 2
Input parameters for rotor-bearing system thermal analysis [12].

Parameters	Value
Shaft Radius, R_s [mm]	50.8
Bearing Length, L_b [mm]	50.8
Bearing Clearance, $C_{l,b}$ [mm]	0.0749
Pad Thickness, t_p [mm]	12.7–15 (at pivot)
Pad Arc Length, l_p [degree]	60
Applied Load, w [N]	5000
Preload, m_{pr}	0.5
Operating Speed, Ω_s [kRPM]	3–15
Outside H.T.C., h_∞ [W/m^{2}K]	50
Ambient Temperature, T_∞ [C]	30
Supply Oil Temperature, T_{sup} [C]	40
Pad Flexible Modes Number	1–20
Lubricant type	ISO 32
Material of Solid Domains	Steel

*H.T.C.: Heat transfer coefficient

end seals heat up the shaft and pads considerably. Interestingly, the small orifice reduces the shaft and pad temperatures more than that of the large orifice because of the intense oil penetration effect in the groove with the small orifice. The cooling of the solid domains contributable to the groove region mixing can be strengthened by increasing the supply flow rate, as represented in Fig. 19(a) and (b). If a LEG is utilized with the close-end seals, its cooling ability is ineffective, as shown in Fig. 19(2) and (3), which is similarly observed in the experimental study [22].

Fig. 20 shows the effect of oil injection type on the bearing stiffness and damping constants, which are critical parameters for determining rotordynamic stability and critical speeds. The dynamic coefficients tend to increase with decreased film thickness [11]. As seen in Fig. 22(a), increased thermal expansion at higher operating speed makes the fluid-film thinner, yielding higher stiffness and damping coefficients. As shown in Fig. 22(a), the increased thermal expansions at higher operating speed makes the fluid-film thinner. This yields higher stiffness and damping coefficients. As shown in Fig. 22(b) and (c), the averaged film thickness reductions caused by the pad and journal's thermal expansion are more significant at higher operating speeds. In contrast, the strong cooling effect of oil injection, like direct lubrication with the open-end seals, decreases the thermal expansions of the shaft and pads, resulting in lower stiffness and damping coefficients. It is notable that the supply flow rate does not have a significant effect on the dynamic coefficients, as shown by comparing Fig. 20(a) and (b).

Fig. 21 represents the extruded computational domains and 3D temperature distribution when the shaft rotates at 15,000 RPM (Case 1). The proposed model is compared to the conventional approaches with mixing coefficients 0.4 and 1.0. It is important to understand the heat transfer mechanism for reliable thermal analysis of the rotor-bearing system. The viscous heating produces the primary heat in the thin film, and the generated heat is transported in the circumferential direction by the rotating shaft while diffusing the heat to the shaft and pads. The shaft and pad outer surfaces are exposed to ambient conditions, and the shaft and pads are cooled via convective heat transfer. The advection heat transfer in the radial direction is negligible in the fluid film. Advection heat is transported in the circumferential direction, and the groove mixing with the cold supply oil cools down this hot oil flowing from the previous pad's trailing edge. Although mixing in the groove region is a localized effect, it can significantly impact the overall 3D temperature distribution of the rotor-bearing system because of the fast rotating shaft (large, circulating circumferential advection heat). For instance, the temperature distributions are very different for the groove mixing models, as shown in Fig. 21.

The proposed model that employs the deep learning groove mixing model predicts the temperature contour reasonably, as

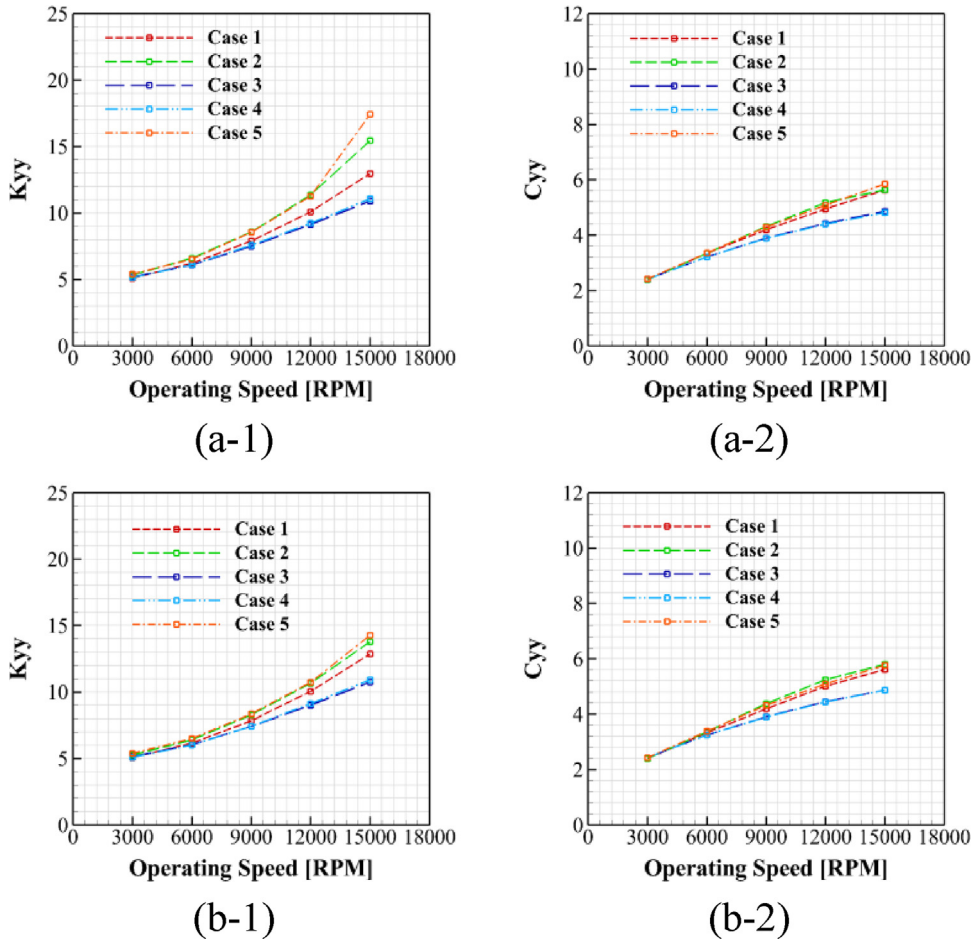

Fig. 20. Non-dimensional dynamic coefficients for various injection types; (a) 35 LPM, (b) 52.5 LPM; (1) non-dimensional stiffness coefficient (K_{yy}), (2) non-dimensional damping coefficient (C_{yy}),; Case 1: small 1 orifice-closed seal, Case 2: large 1 orifice-closed seal, Case 3: 1 nozzle-open seal, Case 4: 3 nozzles-open seal, Case 5: LEG-closed seal.

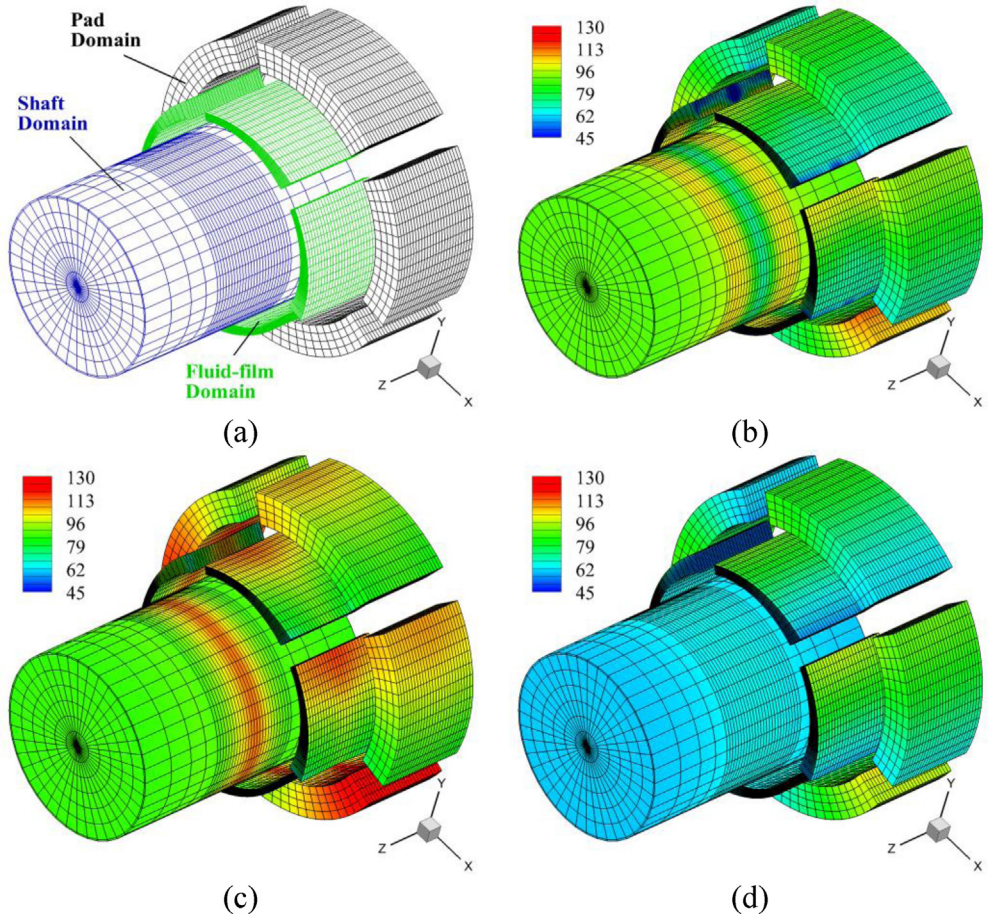

Fig. 21. 3D Temperature distribution at 15,000 RPM (Case 1, 35 LPM); (a) rotor-bearing's extruded view, (b) deep learning groove mixing, (c) 1.0 mixing coefficient, (d) 0.4 mixing coefficient.

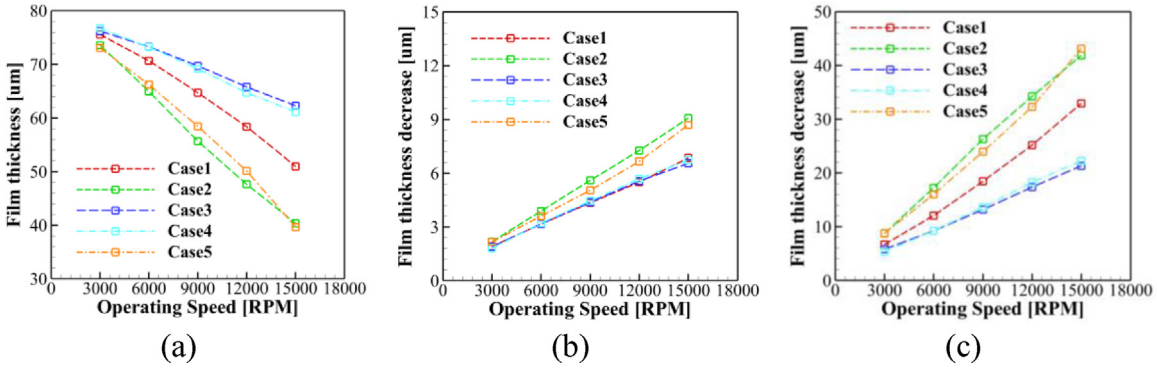

Fig. 22. Net averaged film thickness (a) and the decreases in film thickness due to pad (b) and journal (c) thermal expansions.

shown in Fig. 21(b). The shaft temperature at the bearing mid-span is lower because of the penetration of the supply oil to the shaft surface. Also, the other shaft temperatures in the bearing region are higher. This is because the thermal mixing effect is minor near the shaft surface, except for the oil injection region, as represented in Fig. 12(b) and (c). Moreover, the temperature solutions in Fig. 21(b) have similar distribution with the full-CFD results presented in [10]. The axisymmetric journal temperature distribution in the new model follows the well-established convention for determining stiffness and damping.

Fig. 23 shows the 3D temperature contour of the rotor-bearing system for the five oil injection cases treated in this study. It is clearly observed that the direct lubrication with the open-end seals, as shown in Fig. 23(c) and (d), has superior cooling ability since the supply oil is most effectively mixed with the hot oil, as confirmed in Fig. 13(2) and 15(1). As shown in Fig. 23(a) and (e), it is seen that a groove with a small diameter orifice (or nozzle) and close-end seal shows considerable temperature variation in the axial direction, due to the intense supply oil penetration to the shaft surface.

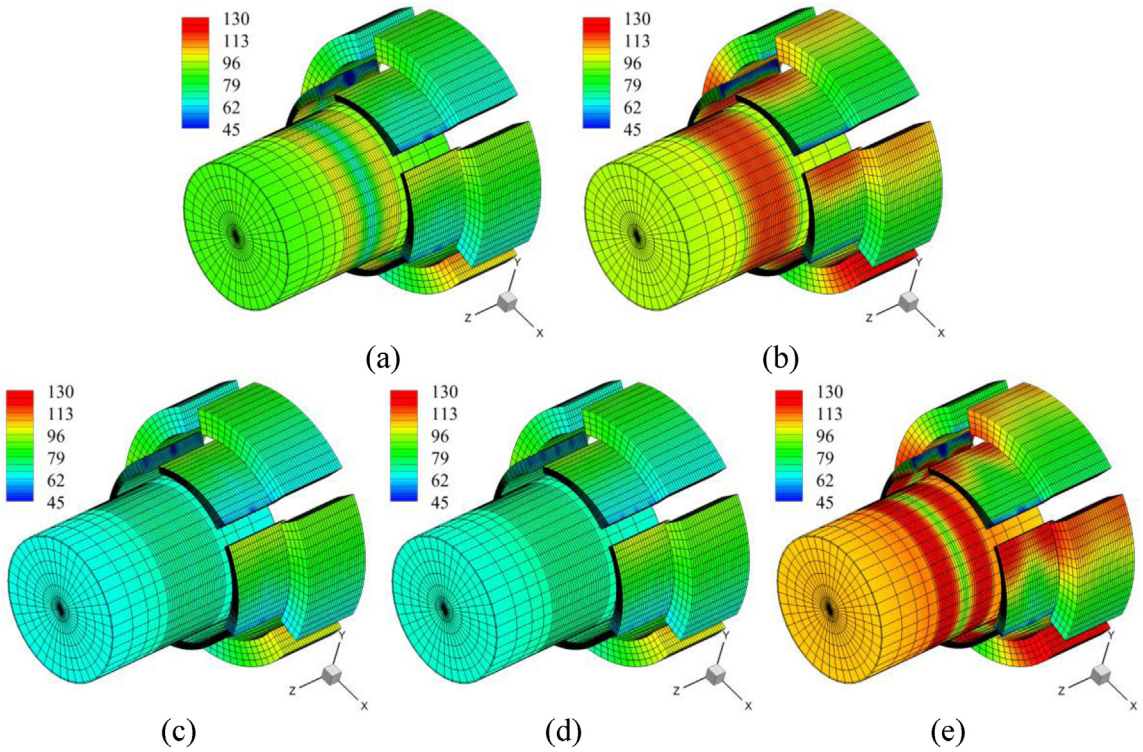

Fig. 23. 3D Temperature distribution with 35 LPM supply oil flow and 15,000 RPM; (a) Case 1: small 1 orifice-closed seal, (b) Case 2: large 1 orifice-closed seal, (c) Case 3: 1 nozzle-open seal, (d) Case 4: 3 nozzles-open seal, (e) Case 5: LEG-closed seal.

4. Conclusion

This paper presented a novel thermal mixing model for a tilt pad journal bearing, via a deep convolutional autoencoder trained with numerous CFD model predictions. The groove region of the tilt pad bearing consists of the oil supply inlet (orifice or nozzles), moving-wall (rotating shaft), circumferential groove inlet and outlet, and axial side outlets. The groove's thermal model is utilized to predict the temperature distribution at the circumferential groove outlet (pad leading edge of fluid-film) in the rotor-bearing system.

The groove thermal mixing model in conventional approaches [1–4] has significant pitfalls that ignore the 2D temperature distribution effect, and employ uncertain parameters such as the mixing coefficient and groove efficiency parameter. The CFD-based rotor-bearing model, which solves the full Navier-Stokes equation for the fluid-film domain, provides an alternative approach. Its shortcoming though is prohibitive computation time when directly embedded into a rotor bearing system model. Thus, in this study, the proposed Reynolds-based rotor-bearing model, which solves the Reynolds equation with respect to the fluid-film domain without loss of prediction accuracy, was combined with the trained deep convolutional autoencoder that acts as the surrogate groove model. The detailed modeling methodology was elaborated in Section 2.

Five oil injection cases were treated in this research, including direct (nozzle with open-end seal) and flooded (orifice with close-end seal) lubrication. The CNNs as the surrogate groove model were trained for each oil injection case based on CFD-generated data. The input design space of the training data set was derived from the combinations of the full factorial and Latin Hypercube Sampling method. The test dataset was generated from randomly extracted input combinations. The trained CNNs through deep learning showed excellent regression performance for the training and test dataset when comparing the CNN and CFD predictions for the non-dimensional 2D temperature distribution at the circumferential groove outlet.

The various temperature distribution patterns emphasize the importance of including the 2D pad inlet temperature distribution since it can directly affect heat transfer to the shaft and pad. The effectiveness of combining the Reynolds model with the trained CNN has been verified by comparing results with a full CFD model [12], for a rotor-bearing system. The proposed model and CFD model showed good agreement for the eccentricity ratio, shaft temperature, pad temperature, and dynamic coefficients. In addition, the comparison between the proposed model and experimental data [19] proved the validity of the suggested model.

The proposed and conventional model results were compared for thermal analysis of the rotor-bearing system with five oil injection cases. The results showed the direct lubrication with open-end seals has the superior cooling capability for the rotor-bearing system. The simulation results confirmed that the conventional groove model has significant uncertainty depending on the assumed mixing coefficient or groove efficiency parameter, and consequently questionable 3D temperature distribution can be predicted for the entire rotor-bearing system. This illustrates the importance of the proposed model, which provides a reliable temperature distribution effect at the pad leading edge of the fluid film. The proposed model makes it possible to accurately and efficiently conduct a thermal analysis of a rotor-bearing system, reflecting the characteristics of the various oil injection types.

Declaration of Competing Interest

None.

CRediT authorship contribution statement

Jongin Yang: Conceptualization, Methodology, Software, Writing – original draft, Visualization, Validation. **Alan Palazzolo:** Conceptualization, Writing – review & editing.

Acknowledgment

The authors appreciate the funding from the Texas A&M Turbomachinery Research Consortium (TRC) and the Texas A&M High-Performance Research Computing Center (HPRC).

References

[1] C. Ettles, Hot oil carry-over in thrust bearings, Proc. Inst. Mech. Eng., Conf. Proc. 184 (12) (1969) 75–81.
[2] J. Mitsui, H. Hori, M. Tanaka, Thermohydrodynamic analysis of cooling effect of supply oil in circular journal bearing, ASME J. Lubr. Tech. 105 (3) (1983) 414–420.
[3] J. Suh, A. Palazzolo, Three-dimensional dynamic model of TEHD tilting-pad journal bearing—part I: theoretical modeling, ASME J. Tribol. 137 (4) (2015) 041704.
[4] B. Abdollahi, L. San Andrés, Improved estimation of bearing pads' inlet temperature: a model for lubricant mixing at oil feed ports and validation against test data, ASME J. Tribol. 141 (3) (2018) 031703.
[5] D. Lee, K. Sun, B. Kim, D. Kang, Thermal behavior of a worn tilting pad journal bearing: thermohydrodynamic analysis and pad temperature measurement, Tribo. Trans. 61 (6) (2017) 1074–1083.
[6] L. San Andrés, Y. Li, Effect of pad flexibility on the performance of tilting pad journal bearings—benchmarking a predictive model, ASME J. Eng. Gas Turbines Power 137 (12) (2015) 122503.
[7] S.M. Mehdi, K. Jang, T. Kim, Effects of pivot design on performance of tilting pad journal bearings, Tribol. Int. 119 (2018) 175–189.
[8] H.A.P. da Silva, R. Nicoletti, Design of tilting-pad journal bearings considering bearing clearance uncertainty and reliability analysis, ASME J. Tribol. 141 (1) (2019) 011703.
[9] H. Arihara, Y. Kameyama, Y. Baba, L. San Andés, A thermoelastohydrodynamic analysis for the static performance of high-speed—heavy load tilting-pad journal bearing operating in the turbulent flow regime and comparisons to test data, ASME J. Eng. Gas Turbines Power 141 (2) (2018) 021023.
[10] J. Yang, A. Palazzolo, 3D thermo-elasto-hydrodynamic CFD model of a tilting pad journal bearing—part I: static response, ASME J. Tribol. 141 (6) (2019) 061702.
[11] J. Yang, A. Palazzolo, 3D thermo-elasto-hydrodynamic CFD model of a tilting pad journal bearing—part II: dynamic response, ASME J. Tribol. 141 (6) (2019) 061703.
[12] J. Yang, A. Palazzolo, Computational fluid dynamics based mixing prediction for tilt pad journal bearing TEHD modeling—part I: TEHD-CFD model validation and improvements, ASME J. Tribol. 143 (1) (2020) 011801.
[13] X. Liang, Y. Xie, R. Day, X. Meng, H. Wu, A data driven deep neural network model for predicting boiling heat transfer in helical coils under high gravity, Int. J. Heat Mass Transf. 166 (2021) 120743.
[14] G. Zhu, T. Wen, D. Zhang, Machine learning based approach for the prediction of flow boiling/condensation heat transfer performance in mini channels with serrated fins, Int. J. Heat Mass Transf. 166 (2021) 120783.
[15] Fei, W., Narsilio, G.A., and Disfani, M.M., "Predicting effective thermal conductivity in sands using an artificial neural network with multiscale microstructural parameters," Int. J. Heat Mass Transf., 170, p. 120997.
[16] Bo, Z., Li, H., Yang, H., Li, C., Wu, S., Xu, C., Xiong, G., Mariotti, D., Yan, J., Cen, K., and Ostrikov, K., Combinatorial atomistic-to-AI prediction and experimental validation of heating effects in 350 F supercapacitor modules," Int. J. Heat Mass Transf., 171, p. 121075.
[17] F. Kolodziejczyk, B. Mortazavi, T. Rabczuk, X. Zhuang, Machine learning assisted multiscale modeling of composite phase change materials for Li-ion batteries' thermal management, Int. J. Heat Mass Transf. 172 (2021) 121199.
[18] J. Yang, A. Palazzolo, Computational fluid dynamics based mixing prediction for tilt pad journal bearing TEHD modeling—part II: implementation with machine learning, ASME J. Tribol. 143 (1) (2020) 011802.
[19] C.D. Kulhanek, Dynamic and Static Characteristics of a Rocker-Pivot, Tilting–Pad Bearing With 50% and 60% Offsets, Mechanical Engineering, Texas A&M University, College Station, TX, 2010 M.S. thesis.
[20] K. He, X. Zhang, S. Ren, J. Sun, Delving deep into rectifers: surpassing human-level performance on imagenet classifcation, in: Proceedings of the IEEE International Conference on Computer Vision, 2015, pp. 1026–1034.
[21] F.R. Menter, P.E. Smirnov, T. Liu, F.R. Avancha, A one equation local correlation-based transition model, Flow, Turbul. Combust. 95 (4) (2015) 583–619.
[22] K.B. Bang, J.H. Kim, Y.J. Cho, Comparison of power loss and pad temperature for leading edge groove tilting pad journal bearings and conventional tilting pad journal bearings, Tribol. Int. 43 (8) (2010) 1287–1293.